Available online at www.sciencedirect.com

ScienceDirect

Journal of Magnesium and Alloys 8 (2020) 319–328

www.elsevier.com/locate/jma

Full Length Article

Spark plasma sintering of a high-energy ball milled Mg-10 wt% Al alloy

M.U.F. Khan[a], A. Patil[b], J. Christudasjustus[a], T. Borkar[b], R.K. Gupta[a,*]

[a] Department of Chemical, Biomolecular, and Corrosion Engineering, The University of Akron, Akron, OH 44325, United States
[b] Department of Mechanical Engineering, Washkevicz College of Engineering, Cleveland State University, Cleveland, OH 44115, United States

Received 7 August 2019; received in revised form 30 January 2020; accepted 15 February 2020
Available online 12 May 2020

Abstract

The influence of spark plasma sintering (SPS) temperature on microstructure, hardness and corrosion behavior of a high-energy ball milled Mg-10 wt% Al alloy was investigated in this work. The holding time and sintering pressure for SPS were kept constant while varying the sintering temperature from 200 to 350 °C. The grain size and microstructure were studied using X-ray diffraction analysis, scanning electron microscopy, energy dispersive X-ray spectroscopy, and Archimedes' based density measurement. Corrosion behavior was investigated using potentiodynamic polarization tests. The nanocrystalline regime (grain size < 100 nm) was maintained even after SPS up to 350 °C. The density of the alloy increased with increasing the SPS temperature. Vickers' hardness and corrosion performance improved up to 300 °C followed by a decrease after SPS at 350 °C. Possible reasons for densification, strengthening, and corrosion behavior have been discussed in the light of reduced porosity and microstructural changes.

Keywords: Nanocrystalline alloy; Magnesium; High energy ball milling; Spark plasma sintering; Corrosion.

1. Introduction

In this era of limited non-renewable resources, stronger, durable and lightweight materials will aid in reducing material consumption and necessity for production. Mg with a density of ~1.7 g/cm^3 has the potential to come up as a structural material with the highest strength-to-weight ratio. However, Mg still needs to compete with other structural materials such as Fe-based and Al-based alloys for high strength and corrosion resistance. The properties of the Mg alloys produced by conventional production methods such as casting has been restricted due to constraints posed by limited grain refinement and solid solubility of the desired alloying elements, and formation of intermetallic phases etc. [1]. Non-conventional manufacturing technologies have the potential of producing alloys exceeding the strength of alloys produced by conventional methods [2–9], which open up avenues for cost saving in automotive, aerospace, and several other industrial applications by developing lightweight materials with higher achievable strength [1,10,11].

Non-conventional manufacturing techniques such as sputter deposition [7,12] and rapid solidification [13,14] provide the benefit of achieving high solid solubility of the alloying elements and, therefore, high corrosion resistance and strength. However, engineering applications of these techniques are limited because of challenges in upscaling the production. Several processing techniques involving severe plastic deformation (SPD) for material strengthening are equal-channel angular pressing (or extrusion) [15–17], high pressure torsion, [6,17–19] and surface mechanical attrition treatment [20–22]. SPD techniques produce alloys with fine grains (<1 μm) [18,23], containing a significant fraction of grain boundaries that hinder the movement of dislocations [15], and improves the strength. Mechanical alloying or high-energy ball milling (HEBM) [17,23,24] has been used for synthesizing a wide range of materials including oxide dispersion strengthened materials [25], ceramics [26,27], intermetallic compounds [28–30], nanocomposites [31,32], high entropy alloys [33–35] and nanocrystalline alloys [36–38]. HEBM has also

* Corresponding author.
E-mail address: rgupta@uakron.edu (R.K. Gupta).

https://doi.org/10.1016/j.jma.2020.02.006

been reported to be capable of inducing grain refinement below 100 nm as well as producing supersaturated solid solutions [24,39,40]. Recent work on Fe [41–43] and Al [39,44] based alloys have demonstrated that HEBM could improve both corrosion resistance and strength. Grain refinement below 100 nm, extended solid solubility of alloying elements and uniform dispersion of refined second phases were attributed to improved corrosion resistance and mechanical strength.

High-energy ball milled (HEBMed) alloys are often in the powder form, which needs to be consolidated into fully dense alloys for investigating their properties and furthering in engineering applications. Most of the consolidation methods need exposure to high temperatures. Grain growth and decomposition of a supersaturated solid solution to the thermodynamically stable phases upon high temperature exposure is inevitable; however, the kinetics can be impeded by choosing lower temperatures [24,45,46]. Therefore, consolidation methods requiring low temperature and short time are sought for the consolidation of the HEBMed alloys.

Spark plasma sintering (SPS) [47], a widely used technique in consolidating powder materials including metals, ceramics, and composites [48,49], is reported to result in densification in a shorter time and lower temperatures [49]. The process of SPS involves the densification of powder materials by applying electric current in the range of 100 A/cm^2; however, only a fraction of it flows through the material. The electric current heats the material due to resistance offered by the powder contacts and space between them [50]. It allows a heating rate of up to about 1000 K.min^{-1} as compared to that of hot pressing, which offers 5–10 K.min^{-1} [51]. SPS allows fast densification at lower temperatures in contrast to conventional methods of sintering, resulting in the retention of nanocrystalline structure and non-equilibrium alloys produced by HEBM, and associated properties [51,52]. The rapid heating rates allow densification by minimizing any surface diffusion of the materials during heating that is suggested to hinder densification [51,53]. This process also helps in retaining the refined grain size, which is obtained after significant refinement achieved due to milling [54]. The grain growth can be minimized by controlling the consolidation parameters, e.g. time and temperatures. Therefore, there is merit in optimizing the SPS process parameters to produce fully dense nanocrystalline alloys with extended solid solubility. SPS has been applied to commercial Mg alloys such as AE42 [55], AZ31 [56,57], and AZ91 [58]. Recent work on HEBMed Mg–Al alloy has shown improvement in the strength after sintering [59]. Present work attempts to improve the consolidation of HEBMed nanocrystalline Mg-10 wt% Al alloy powder using SPS, thereby aiming towards better mechanical and corrosion properties. Variation in the microstructure, hardness, density, and corrosion parameters after SPS at different temperatures have been discussed. This study could assist and form the basis for the selection of optimized SPS processing parameters for future researchers in order to obtain desired microstructures and mechanical properties for Mg–Al based alloys.

2. Experimental

2.1. Material

The Mg (99.8%, 40–80 mesh) and Al (99.7%, −50/+100 mesh) powders were obtained from Fisher Scientific. The powders in the weight ratio Mg/Al: 9/1 along with 1.5 wt% stearic acid as process controlling agent were placed in the milling jars in an inert gas (high purity Ar atmosphere, O_2 < 25 ppm). The ball to powder weight ratio was 40:1, and the ball milling speed was 280 rpm. The milling was performed in tungsten carbide (WC) jar containing WC balls of 10 mm in diameter. The milling time was 100 h with a pause time of 30 min after every hour of milling, and finally, the jar was opened in an Ar atmosphere. The milling process was the same as described for the previous work on Mg–xAl alloys [59].

2.2. Consolidation by spark plasma sintering (SPS)

The high-energy ball-milled Mg-10 wt% Al alloy powder was consolidated using Thermal Technology SPS 10–3 machine at various temperatures- 200, 250, 300, and 350 °C- under uniaxial pressure of 1 GPa in WC die of 10 mm diameter. A graphite sheet was placed in between the powder, die, and punches to avoid sticking along with ensuring electrical conductivity. The heating rate for achieving the SPS temperature was 50 °C/min, the hold time for SPS was 5 min, and a cooling rate of 999 °C/min was allowed after the release of the pressure from punches. For comparison, the milled alloy was also cold compacted using hydraulic press under 3 GPa pressure at room temperature (25 °C) for 10 min.

2.3. Characterization using X-ray diffraction (XRD), scanning electron microscopy (SEM), and energy-dispersive X-ray spectroscopy (EDXS)

The spark plasma sintered samples were ground to 1200 grit SiC paper for XRD analysis and polished up to 0.05 μm finish using diamond suspensions followed by colloidal silica + alumina suspension for SEM/EDXS studies. After grinding and polishing, the samples were ultrasonically cleaned for 5 min with ethanol and also following each subsequent polishing step.

The spark plasma sintered (SPSed) alloy samples were analyzed using a Rigaku X-ray diffractometer for phase and grain size determination. The diffractometer had Cu-K_α radiation source ($\lambda = 0.1541$ nm), which was used to perform the XRD at a tube voltage of 40 kV and a tube current of 44 mA with a scan rate of 1°/min for the Mg-10 wt% Al alloy SPSed at four temperatures. The grain size was calculated using Scherer's equation [60] for three highest intensity peaks after removing the instrumental broadening, which was determined using annealed pure Mg powder.

The microstructure of SPSed alloys was performed using a Tescan Lyra 3 FIB-FESEM system in backscattered electron (BSE) mode with an accelerating voltage of 20 kV while

maintaining a working distance of 9–10 mm. EDXS was also performed in the same instrument to analyze the composition of different phases present in the microstructure.

2.4. Density

The experimental density of consolidated samples by cold compaction (CC) and SPS was determined using Sartorius Quintix65-1S semi-micro balance equipped with a YDK03 density kit attached. The temperature of the deionized water was measured and accounted for every density measurement, and all the samples were ground up to 1200 grit size SiC paper. The density measurements were repeated five times.

2.5. Hardness

The SPSed alloys were ground up to 1200 grit size SiC before hardness measurements. Hardness was measured using Vickers microindenter (Buehler-Wilson Tukon 1202) by applying 50 gf load with a dwell time of 10 s, where ten measurements were taken for each sample while maintaining the distance between any two indents > 5 times of the indent size.

2.6. Potentiodynamic polarization (PDP)

The corrosion behavior of Mg-10 wt% Al alloy SPSed at the four temperatures was investigated by potentiodynamic polarization (PDP) test using a VMP-300 potentiostat from Biologic. All samples were ground up to 1200 grit SiC paper. PDP tests were carried out in a conventional three-electrode setup using a flat cell from Princeton Applied Research having platinum mesh as a counter electrode. A standard calomel electrode (SCE) was used as a reference, and sample under study as a working electrode. All tests were performed in 0.1 M NaCl solution exposed to air at room temperature (25 °C). The open circuit potential (OCP) of the samples was monitored for 20 min before commencing the PDP tests. Potential scans started from 250 mV below the OCP. The potential was increased with a scan rate of 1 mV/s until an anodic current reached 10 mA/cm^2. PDP tests were performed at least three times.

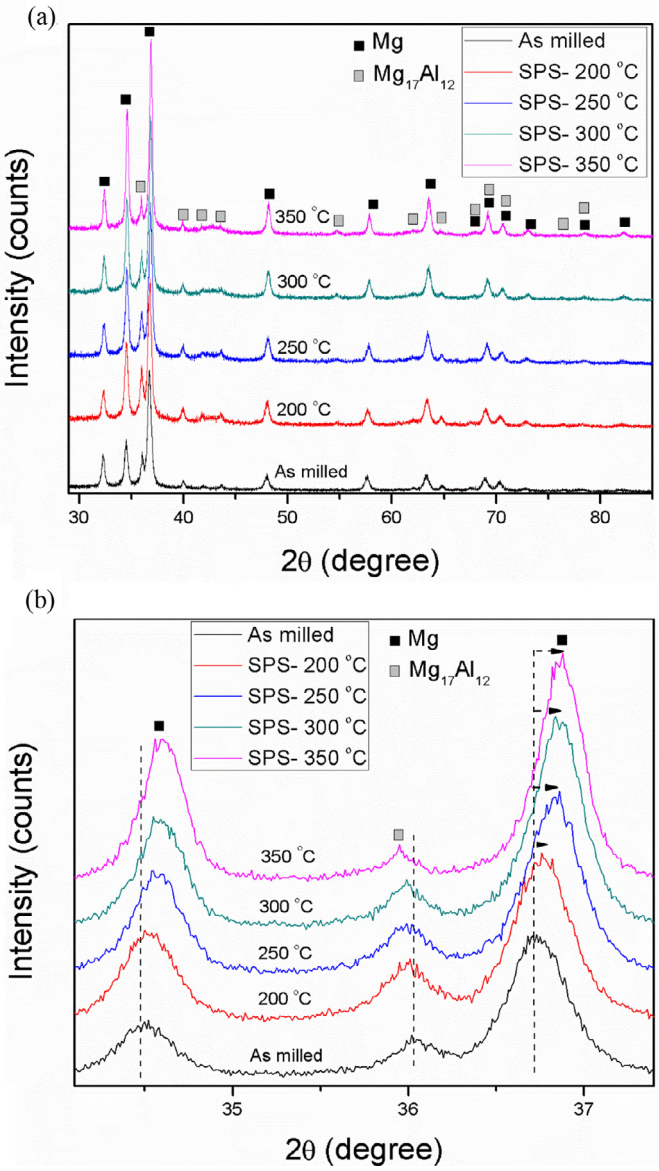

Fig. 1. XRD scans for high-energy ball milled (HEBMed) Mg-10 wt% Al alloy with full scan in (a) showing presence of dual phase and zoomed-in region in (b) showing the effect of spark plasma sintering (SPS) temperature on the peak position and intensity for Mg and $Mg_{17}Al_{12}$ phases. The arrows indicate peak shift for Mg towards higher 2θ values with increasing SPS temperature.

3. Results

3.1. X-Ray diffraction

X-ray diffraction scans for SPSed Mg-10 wt% Al are shown in Fig. 1. A zoomed-in region has been shown in Fig. 1b. Phase analysis suggested the presence of Mg and $Mg_{17}Al_{12}$ phases. There are two major observations to notice. Firstly, the peak intensity of the two phases was dependent upon the SPS temperature. The peak intensity for Mg increased whereas that for $Mg_{17}Al_{12}$ intermetallic decreased on increasing the SPS temperature. The decrease in area under the peak suggests a decrease in the volume fraction of the phase. Therefore, the decrease in the area under the $Mg_{17}Al_{12}$ phase peak, indicated by a decline in the intensity and narrowing of peaks (Fig. 1), suggests a lowering of its volume fraction. Secondly, the broadening of peaks for both the phases decreased with an increase in the SPS temperature (Fig. 1a). The decrease in peak broadening indicates an increase in the crystallite size. The crystallite size for Mg-10 wt% Al alloy after SPS, at temperatures between 200 and 350 °C, has been compared with that of a cold compacted sample (Fig. 2). The average crystallite size of the alloy in as milled condition was 44 ± 10.3 nm, which increased to 51.3 ± 3.4 nm after SPS at 250 °C. A rapid growth in crystallite size was observed after SPS at 250 °C. Crystallite size increased to 82.9

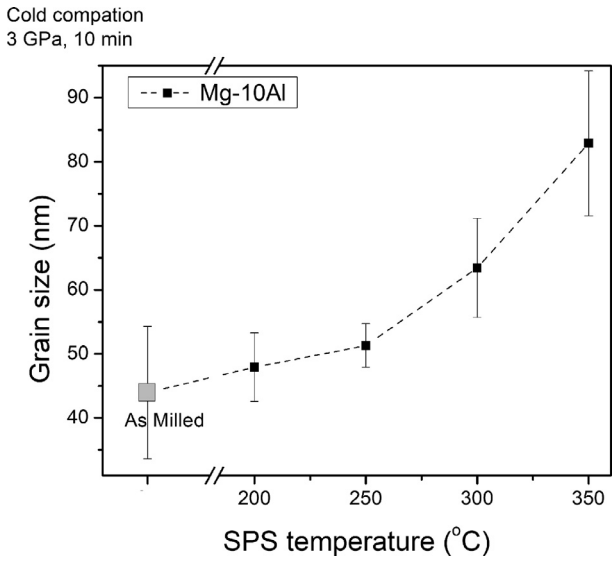

Fig. 2. Influence of the SPS temperature on the grain size of HEBMed Mg-10 wt% Al alloy after consolidation.

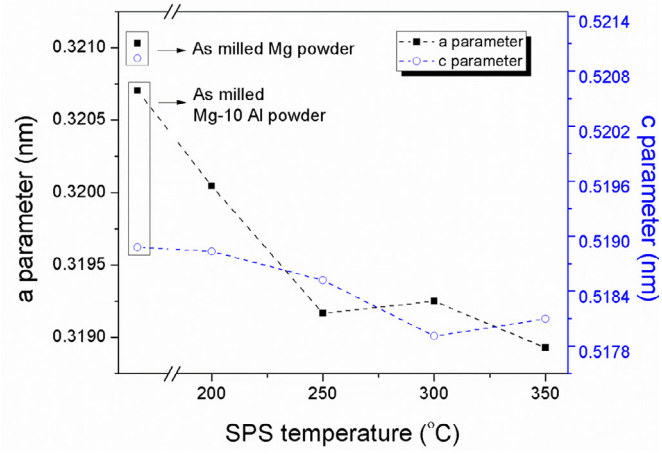

Fig. 3. Lattice parameters "a" and "c" for HEBMed Mg-10 wt% Al after cold compaction and spark plasma sintering at different temperatures with 1 GPa pressure. Lattice parameters for as milled Mg are also shown for comparison.

± 11.3 nm after SPS at 350 °C. Retaining the crystallite size of Mg-10 wt% Al under 100 nm even after SPS at 350 °C is remarkable.

Fig. 1b shows that the Mg peaks shifted towards higher 2θ values, which refer to a decrease in the lattice parameter. The lattice parameter variation of the SPSed Mg–10Al alloys have been shown and compared with as-milled Mg and Mg-10 wt% Al alloy in Fig. 3. Both 'a' and 'c' parameters for as milled Mg-10wt% Al were smaller than those of as-milled Mg. This decrease in lattice parameters indicated the formation of Mg-Al solid solution due to the ball milling. The solid solubility of Al in ball milled Mg-10 wt% Al alloy, using a change in lattice parameter 'c', was determined to be 4% [61]. Both the lattice parameters, 'a' and 'c', decreased further with an increase in the SPS temperature (Fig. 3). The decrease in both lattice parameters suggests a contraction of Mg lattice due to the increase in the solid solubility of Al with increasing SPS temperature [62]. An increase in Al solid solubility in Mg with increasing temperature has been predicted using PANDAT software [59].

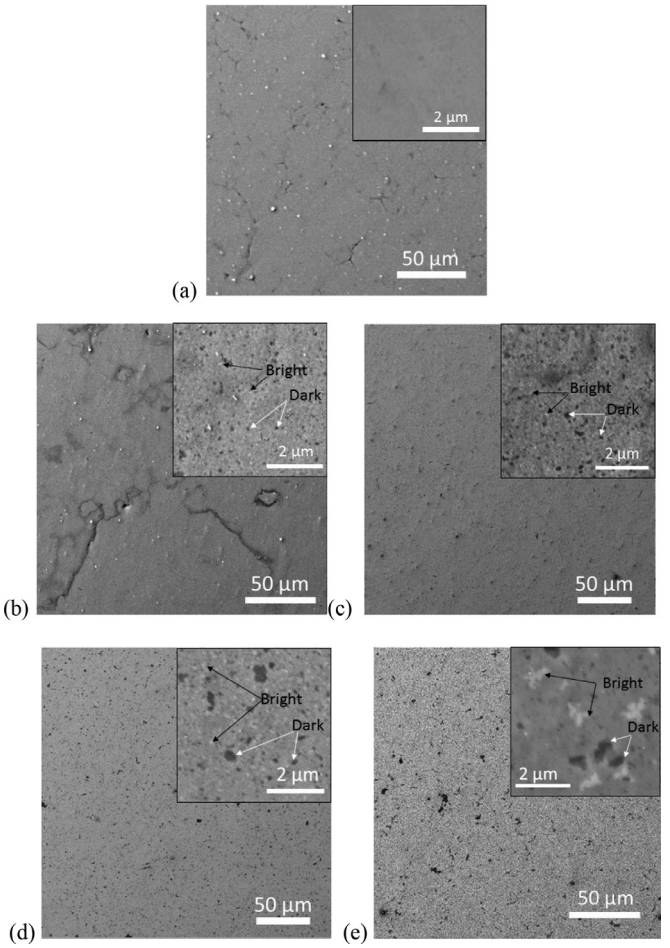

Fig. 4. Microstructure of HEBMed Mg-10 wt% Al alloy after cold compacted condition (a), and after SPS at 200, 250, 300 and 350 °C in (b), (c), (d) and e) respectively. Typical bright regions and dark regions in b-e have been marked with black and white arrows respectively.

3.2. SEM/EDXS

The microstructures of Mg-10 wt% Al alloy samples studied using back-scattered electron (BSE) imaging are shown in Fig. 4. The high magnification BSE images are presented in insets. Fig. 4a presents microstructure for the alloy consolidated at room temperature, whereas Fig. 4b-e shows microstructures of the alloy sintered at different temperatures. Porosity and interparticle boundaries were observed in the samples after cold compaction (Fig. 4a) and SPS at 200 °C (Fig. 4b). Pores and interparticle boundaries were unnoticeable in the samples produced by SPS at or above 250 °C (Fig. 4c-e).

The high magnification images (presented in the insets of Fig. 4) indicate compositional homogeneity of the alloy after cold compaction, whereas a heterogeneous microstructure, marked with bright and dark regions due to the compositional

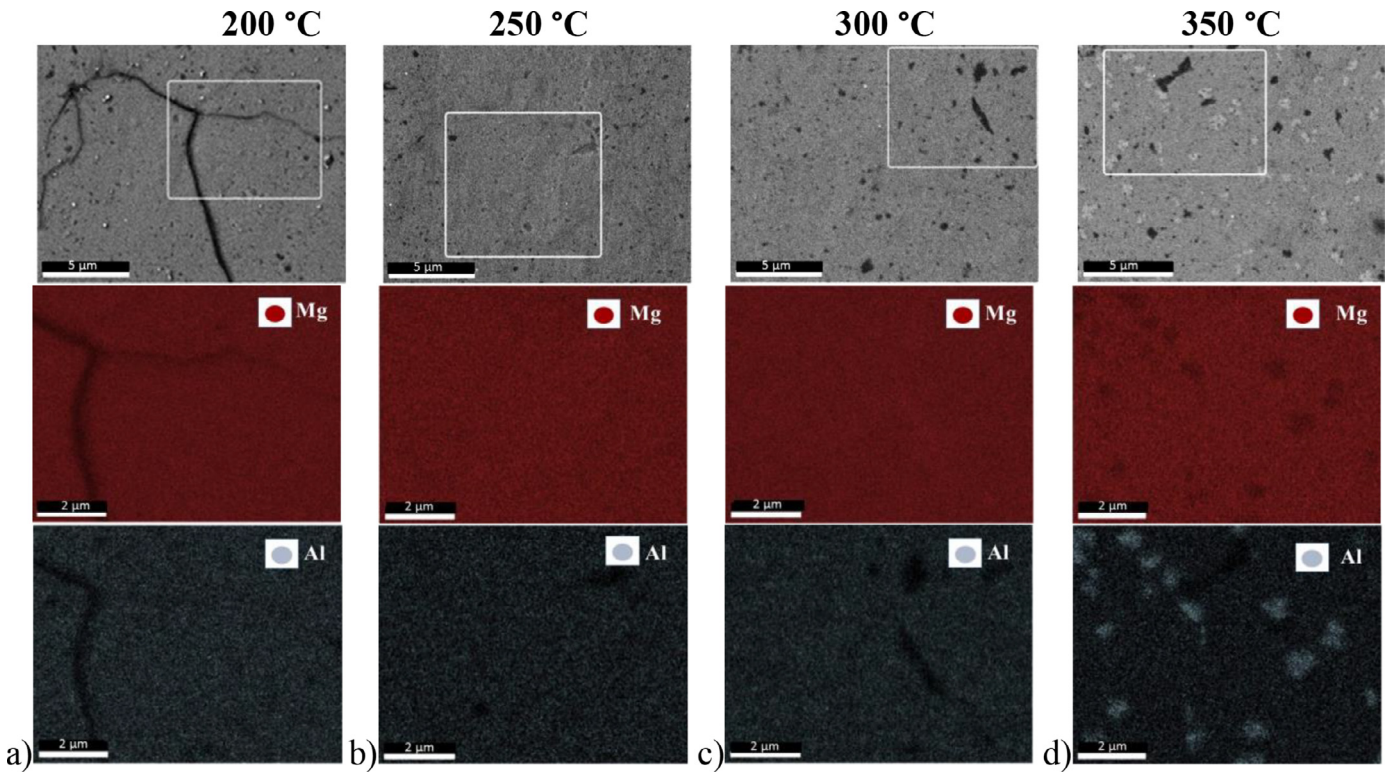

Fig. 5. Energy dispersive X-ray spectroscopy analysis area maps for Mg-10 wt% Al after SPS at (a) 200 °C, (b) 250 °C, (c) 300 °C, (d) 350 °C.

contrast, has been observed in all SPSed samples. The SPS at 200 °C instigated elemental diffusion leading to the emergence of bright particles along with dark regions well distributed in the matrix (Fig. 4b inset) and are indicated by arrows. Bright and dark particles became more distinct and coarser with an increase in the SPS temperature. The size of bright particles was below 200 nm until 300 °C, which increased to 0.8 ± 0.18 µm at 350 °C. With increasing SPS temperature, a decrease in the number density of bright and dark regions was noticed, which indicated the coalescence of these phases leading to coarsening at the expense of neighboring particles.

The BSE images along with EDXS area maps, showing the distribution of the elements, for the alloy SPSed at various temperatures, have been shown in Fig. 5. Mg and Al were uniformly distributed after SPS at 200 °C (Fig. 5a). The dark and bright phases started appearing after SPS at 250 °C (Fig. 5b). The EDXS analysis performed on the two phases and matrix revealed the bright phases to be Al rich while the dark phases were Al lean. Size of the Al rich phase increased with the SPS temperature.

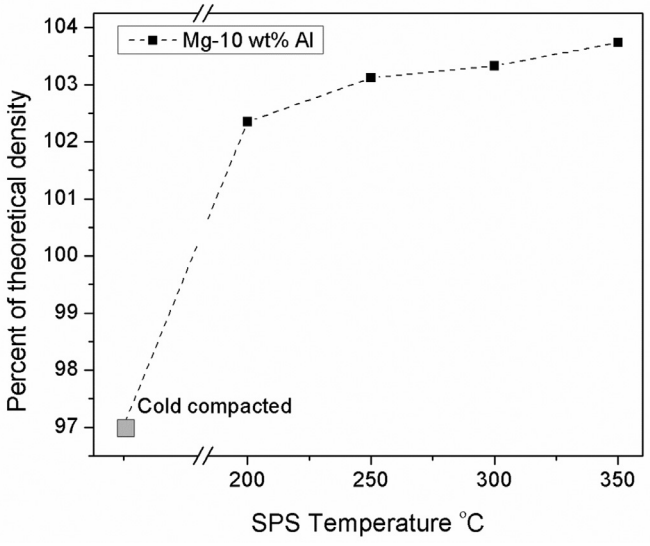

Fig. 6. Measured density (using Archimedes principle) as a percent of theoretical density (from rule of mixture) for cold compacted and spark plasma sintered Mg-10 wt% Al alloys.

3.3. Density

Fig. 6 shows the experimental density along with the theoretical density vs. SPS temperature plot for Mg-10 wt% Al in SPS processed and cold compacted condition. The theoretical density obtained by the rule of the mixture is 1.802 g/cm^3. The experimental density for the cold compacted alloy was lower than the theoretical density, which was attributed to the presence of pores (Fig. 6). The experimental density of the alloy increased with an increase in the SPS temperature, which could be attributed to better densification. Densification increases with increase in SPS temperatures [51,63]. Interestingly, the experimental density of all SPS processed alloys was significantly higher than the theoretical density which could be attributed to the lattice contraction (Fig. 4) and the formation of $Mg_{17}Al_{12}$ intermetallic having a higher density

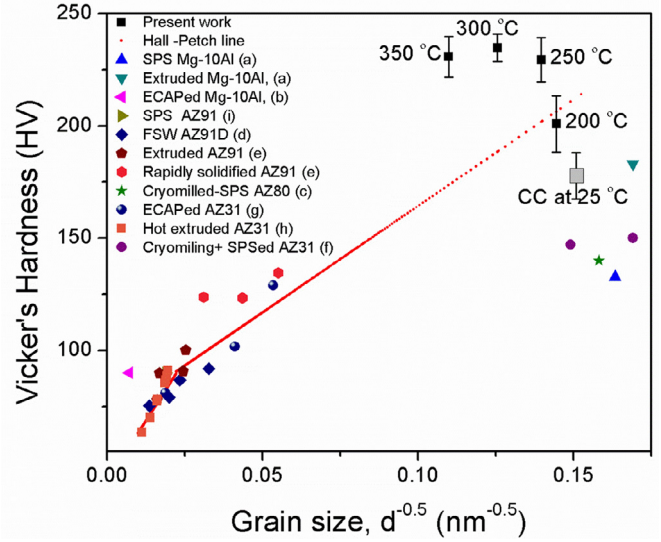

Fig. 7. Influence of SPS temperature on Vickers hardness of HEBMed Mg-10 wt% Al alloy. Hardness for cold compacted alloy of same chemical composition and predicted hardness based on Hall–Petch relationship suggested by Razavi et al.[42]. is also shown for the comparison. The hardness of Mg-10Al (a[65],b[66]), and AZ series alloys (c[2], d[67], e[68], f[69], g[70], h[71], i[58]) reported in the literature has also been compared.

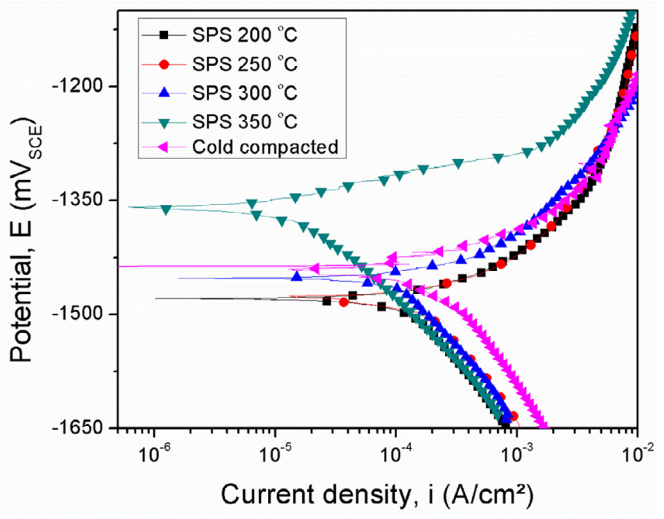

Fig. 8. Potentiodynamic polarization curves for HEBMed Mg-10 wt% Al alloy showing the effect of SPS temperature on the corrosion behavior.

[64], which needs further investigation. Both of these factors are not considered while calculating the theoretical density using the rule of mixture. A precise calculation of the theoretical density of the alloy was not possible due to uncertainty in determining the volume fraction of intermetallic formed and the solid solubility of Al.

3.4. Hardness

The hardness for the Mg-10 wt% Al alloy processed via SPS between 200 and 350 °C has been plotted as a function of grain size (Fig. 7). Hardness of Mg-10Al [65,66] and AZ series alloys [2,58,67–71] produced by SPS and other techniques reported in the literature has also been included in Fig. 7. The hardness of the cold compacted alloy is also included for comparison. The hardness of the alloy SPSed at 200 °C was 200.9 ± 12.5 HV, which is higher than the cold compacted Mg-10 wt% Al (177.9 HV ± 10.33). The hardness of the alloy SPSed at 250 °C increased significantly, followed by a sluggish increase at 300 °C and reaching 234.8 ± 6.1 HV. However, alloy sintered at 350 °C has a lower hardness (230.8 ± 9.0 HV) than that of 300 °C.

The hardness of the alloys increased with an increase in grain size, which is contrary to the Hall–Petch relationship (Fig. 7). The hardness of the alloy, SPSed at various temperatures, was predicted using Hall–Petch relationship suggested by Razavi et al. [70] (for Mg alloys processed by equal channel angular pressing) and shown in Fig. 7. The Hall–Petch relationship given by Razavi et al. [70] for up to 2 μm and above 2 μm are written as Eq. (1) and (2):

$$\sigma_y = 208 + 90d^{-0.5} \quad (1)$$

$$\sigma_y = 124 + 205d^{-0.5} \quad (2)$$

where σ_y is the yield stress, and d is the crystallite size in the metal/alloy.

It can be seen that the hardness predicted by the Hall–Petch relation, as suggested in the literature [70], decreases with an increase in the SPS processing temperature (Fig. 7), primarily due to increasing grain size. In contrast, the experimental hardness values, as well as grain size, increased after SPS. This anomaly indicates the possibility of additional hardening mechanisms. The solubility of Al has been reported to increase with increasing sintering temperatures, and therefore solid solution strengthening increases with increasing SPS temperature [59]. Moreover, age hardening has been suggested to improve the strength of Mg alloy by precipitates formed due to phase transformation [72,73]. Similarly, precipitates were observed after SPS processing (Section 3.2), which are expected to contribute to precipitate strengthening due to the Orowan mechanism [73]. Thus, these two additional mechanisms would have increased the hardness of the alloy after SPS even though the grain size increased.

3.5. Potentiodynamic polarization (PDP) tests

The electrochemical behavior of the SPSed Mg-10 wt% Al was studied using PDP tests in 0.1 M NaCl. Typical potential vs. current density curves obtained from the PDP of the alloy SPSed at various temperatures are presented in Fig. 8. The cathodic current density for the cold compacted alloy was higher than those of SPSed alloys. However, the cathodic current density was not significantly affected by the SPS temperature. The anodic current density remained similar for the lower two temperatures and decreased a little for 300 °C, followed by a significant decrease for sample processed at 350 °C. The corrosion potential (E_{corr}) vs. corrosion current density (i_{corr}) obtained from Tafel analysis

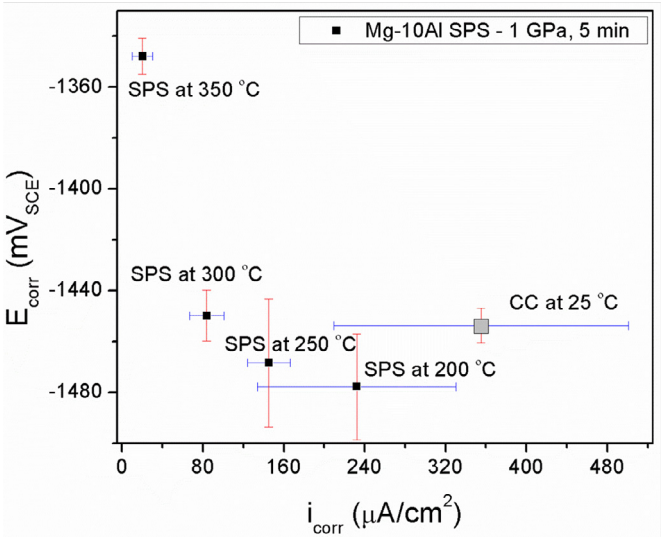

Fig. 9. Influence of the SPS temperature on the corrosion potential (E_{corr}) and corrosion current density (i_{corr}) of HEBMed Mg-10 wt% Al alloy. Cold compacted (CC) alloy is also included for the comparison.

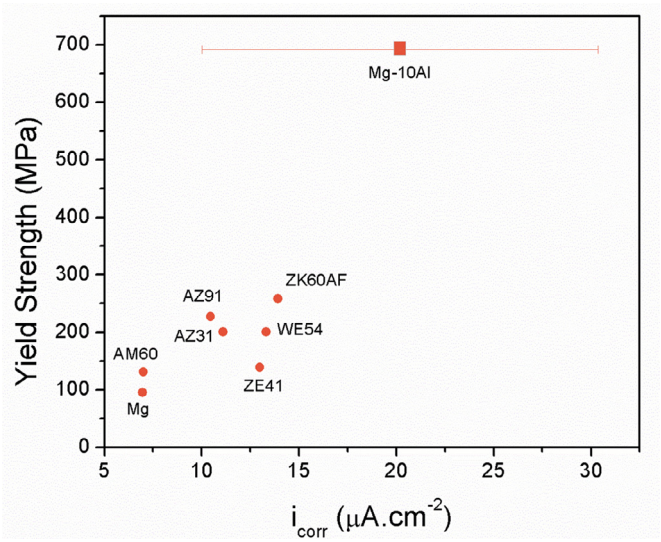

Fig. 10. Corrosion current density vs yield strength for commercial magnesium alloys reported in [50] along with HEBMed Mg-10 wt% Al alloy SPS processed at 300 °C.

has been shown in Fig. 9. The E_{corr} for the alloy increased gradually with an increase in the SPS temperature from 200 to 300 °C, followed by a significant increase for the alloy SPSed at 350 °C. Moreover, i_{corr} decreased with an increase in the SPS temperature from 232.2± 98.3 μA.cm^{-2} at 200 °C to 20.2± 10.2 μA.cm^{-2} at 350 °C. The highest E_{corr} and lowest i_{corr} were observed for Mg-10 wt% Al SPSed at 350 °C.

The error range for both E_{corr} and i_{corr} decreased with increasing SPS temperatures, which could be attributed to the change in the processing defects. Corrosion behavior of SPSed Mg-10 wt% Al alloy can be correlated to the porosity and interparticle boundaries, as discussed in Section 3.2. For cold compaction and SPS at 200 °C, the consolidation was incomplete. Hence unjointed particle boundaries were present which are expected to have a higher dissolution rate because of sharp edges. Such incomplete consolidation would reveal varying areas of open pores during sample preparation and PDP tests, and therefore, a larger variation in the test results is expected.

It is crucial to understand the individual corrosion reactions involved to ascertain the changes in corrosion kinetics. The corrosion of Mg under the neutral pH condition involves dissociation of water molecule causing hydrogen evolution and hydroxyl ion release, which further reacts with the anodic reaction product (bivalent Mg ion) to form $Mg(OH)_2$ as corrosion product [74,75]. The corrosion behavior in Mg alloys is affected by the stability and continuity of the surface film [74]. The kinetics of cathodic reactions are influenced by the presence of regions having potentials noble to that of the Mg matrix. The cathodic kinetics does affect the anodic reaction [76–80], dissolution of Mg, occurring at anodic Mg matrix. Hence, it would be essential to consider the composition, size, and distribution of the cathodic particles in the anodic matrix. The presence of cathodic regions would affect the stable $Mg(OH)_2$ film formation.

3.5.1. Microstructural effects on corrosion properties

The microstructure evolution during consolidation has affected the corrosion behavior of the alloy, depending on the SPS temperature. The grain size was 47.9 ± 5.3 nm (as per Scherrer equation [60]) for the alloys SPSed at 200 °C. Some studies [81,82] suggest that the finer grain size entails higher grain boundary density and increased lattice defects, which led to an increased surface reactivity and, therefore, a higher corrosion rate. On the contrary, several studies [83] have reported improved corrosion behavior with the grain refinement [84]. This ambiguity in the understanding of the effect of grain size has been attributed to the process route implemented for achieving grain refinement [21,83]. Higher corrosion current density for the alloy after cold compaction (Fig. 8) can be attributed to the presence of unjointed interparticle boundaries and pores, which would be dominating over the influence of the grain boundary features.

The combined influence of a) coarsening of Al rich precipitates (Section 3.2, Figs. 4, 5), and b) decrease in the volume fraction of $Mg_{17}Al_{12}$ phase (Fig. 1b), resulted in no significant change in cathodic current kinetics for different SPS temperatures. However, the influence of the $Mg_{17}Al_{12}$ phase on the anodic corrosion current would strongly depend upon their size, distribution, and solubility of Al in the Mg matrix. [85]. It has been suggested that homogeneously distributed fine precipitates in nanocrystalline materials diminishes the microgalvanic interaction, and thus, helps in decreasing the corrosion rate [84,86–88]. Additionally, an increase in the temperature causes an increase in the solid solubility of Al in Mg as indicated by the reduction in lattice parameters (Fig. 4). The alloy SPSed at 350 °C is expected to have the highest solid solubility. Therefore, this increased solid solubility is expected to

increase the corrosion resistance as noticed by E_{corr} and i_{corr} for the alloy SPSed at 350 °C (Fig. 9).

3.6. General discussion- comparison with commercial alloys

The commercial alloys of Mg have not yet made a good position in structural materials. However, the HEBMed Mg–Al alloy presented herein opens up a new opportunity for research in improving the corrosion resistance and mechanical properties of Mg alloys. The hardness and i_{corr} for some of the commercial alloys has been plotted along with HEBMed Mg-10 wt% Al in Fig. 10. It can be seen that the hardness of the Mg-10 wt% Al alloy is superior to commercial alloys [89]. The corrosion current density for HEBMed Mg-10 wt% Al after SPS at 350 °C is comparable with that of commercial alloys. Further research on optimizing the composition of this alloy should lead to the development of high strength and corrosion resistant Mg alloy.

4. Conclusions

Mg-10 wt% Al alloy was produced by high-energy ball milled and subsequent spark plasma sintering at four temperatures (200, 250, 300, and 350 °C). The phase analysis, microstructure, hardness, density, and corrosion behavior of the alloy after spark plasma sintering at four temperatures were investigated. From this investigation, the following conclusions can be outlined:

a. Nanocrystalline Mg-10 wt% Al alloy with a grain size of 44 ± 10.3 nm was successfully produced by high-energy ball milling.
b. The SPS was effective in consolidating the high-energy ball milled alloy powder while retaining nanocrystalline structure. The grain size of SPSed alloy was < 100 nm even after SPS at 350 °C. The density of the alloy increased with an increase in SPS temperature and surpassed the theoretical density, which was attributed to the combined effect of the decrease in lattice parameters due to alloying and formation intermetallic ($Mg_{17}Al_{12}$) exhibiting density higher than the matrix.
c. The HEBMed alloy processed via SPS exhibited higher hardness than that of cold compacted alloy with maximum for the alloy SPSed at 300 °C. The hardness of the alloy processed at various SPS temperatures was higher than the commercial Mg alloys.
d. The corrosion behavior of the alloys improved after SPS as compared to the cold compacted alloy, and lowest corrosion current density was observed for SPS at 350 °C. The improvement in corrosion behavior was attributed to the improved consolidation and increase in the solid solubility of Al in Mg.
e. The hardness of the Mg-10 wt% Al alloy produced via high energy ball milling followed by spark plasma sintering were significantly higher than the commercial Mg alloys, whereas corrosion current density was comparable. Further research on these alloys should lead to Mg alloys with high strength and acceptable corrosion.

Declaration of Competing Interest

There is no conflict of interest.

Acknowledgement

RKG acknowledges the financial support from the National Science Foundation (NSF-CMMI 1846887) under the direction of Dr. Alexis Lewis.

References

[1] I.P. Polmear, Light Alloys - From Traditional Alloys to Nanocrystals, Fourth, Elsevier B.H., Oxford, 2006, doi:10.1017/CBO9781107415324.004.
[2] B. Zheng, O. Ertorer, Y. Li, Y. Zhou, S.N. Mathaudhu, C.Y.A. Tsao, E.J. Lavernia, Mater. Sci. Eng. A 528 (2011) 2180–2191, doi:10.1016/j.msea.2010.11.073.
[3] W. Bin Fang, W. Fang, H.F. Sun, Trans. Nonferrous Met. Soc. China (English Ed. 21 (2011), doi:10.1016/S1003-6326(11)61586-0.
[4] S. Sankaranarayanan, S. Jayalakshmi, M. Gupta, J. Alloys Compd. 509 (2011) 7229–7237, doi:10.1016/j.jallcom.2011.04.083.
[5] H.P. Zhou, L.X. Hu, Y. Sun, H.B. Zhang, C.W. Duan, H. Yu, Mater. Charact. 113 (2016) 108–116.
[6] W.T. Sun, X.G. Qiao, M.Y. Zheng, C. Xu, N. Gao, M.J. Starink, Mater. Des. 135 (2017) 366–376, doi:10.1016/j.matdes.2017.09.048.
[7] E. Juzeliunas, A. Grigucevičiene, K. Leinartas, R. Juškenas, Electrochem. Commun. 6 (2004) 678–682, doi:10.1016/j.elecom.2004.05.005.
[8] Á. Révész, M. Gajdics, L.K. Varga, G. Krállics, L. Péter, T. Spassov, Int. J. Hydrogen Energy. 39 (2014) 9911–9917, doi:10.1016/j.ijhydene.2014.01.059.
[9] X. Du, B. Wu, Sci. China, Ser. E Technol. Sci. 52 (2009) 1751–1755, doi:10.1007/s11431-008-0210-x.
[10] M. Esmaily, J.E. Svensson, S. Fajardo, N. Birbilis, G.S. Frankel, S. Virtanen, R. Arrabal, S. Thomas, L.G. Johansson, Prog. Mater. Sci. 89 (2017) 92–193, doi:10.1016/j.pmatsci.2017.04.011.
[11] C.H. Caceres, Metall. Mater. Trans. A Phys. Metall. Mater. Sci. 38 A (2007) 1649–1662, doi:10.1007/s11661-007-9156-z.
[12] L. Staišiunas, P. Miečinskas, K. Leinartas, A. Selskis, A. Grigucevičiene, E. Juzeliunas, Corros. Sci. 80 (2014) 487–493, doi:10.1016/j.corsci.2013.11.061.
[13] D.H. StJohn, M. Qian, M.A. Easton, P. Cao, Z. Hildebrand, Metall. Mater. Trans. A Phys. Metall. Mater. Sci. 36 (2005) 1669–1679, doi:10.1007/s11661-005-0030-6.
[14] H. Jones, Mater. Sci. Eng. 57 (1983) 22–25.
[15] C.W. Su, B.W. Chua, L. Lu, M.O. Lai, Mater. Sci. Eng. A. 402 (2005) 163–169, doi:10.1016/j.msea.2005.04.035.
[16] J.A. del Valle, F. Carreño, O.A. Ruano, Acta Mater. 54 (2006) 4247–4259, doi:10.1016/j.actamat.2006.05.018.
[17] M.A. Meyers, A. Mishra, D.J. Benson, Prog. Mater. Sci. 51 (2006) 427–556, doi:10.1016/j.pmatsci.2005.08.003.
[18] A. Azushima, R. Kopp, A. Korhonen, D.Y. Yang, F. Micari, G.D. Lahoti, P. Groche, J. Yanagimoto, N. Tsuji, A. Rosochowski, A. Yanagida, CIRP Ann. - Manuf. Technol. 57 (2008) 716–735, doi:10.1016/j.cirp.2008.09.005.
[19] Y. Estrin, A. Vinogradov, Acta Mater. 61 (2013) 782–817, doi:10.1016/j.actamat.2012.10.038.
[20] H... Zhang, Z... Hei, G. Liu, J. Lu, K. Lu, Acta Mater. 51 (2003) 1871–1881, doi:10.1016/S1359-6454(02)00594-3.
[21] C. op't Hoog, N. Birbilis, Y. Estrin, Adv. Eng. Mater. 10 (2008) 579–582, doi:10.1002/adem.200800046.

[22] M. Laleh, F. Kargar, J. Alloys Compd. 509 (2011) 9150–9156, doi:10.1016/j.jallcom.2011.06.094.
[23] C.C. Koch, Nanostructured Mater. 2 (1993) 109–129.
[24] R.K. Gupta, B.S. Murty, N. Birbilis, An Overview of High-energy Ball Milled Nanocrystalline Aluminum Alloys, Springerbrief in materials, Switzerland, 2017, doi:10.1007/978-3-319-57031-0.
[25] P.J. Maziasz, K.F. Russell, M.K. Miller, D.T. Hoelzer, L. Heatherly, E.A. Kenik, Mater. Sci. Eng. A 353 (2003) 140–145, doi:10.1016/s0921-5093(02)00680-9.
[26] R. Lin, F.W. Poulsen, K. Nielsen, R. Clasen, F.J. Berry, J.Z. Jiang, S. Mørup, Phys. Rev. B 55 (2002) 11–14, doi:10.1103/physrevb.55.11.
[27] Z.H. Yang, Y. Zhou, D.C. Jia, Q.C. Meng, Mater. Sci. Eng. A 489 (2008) 187–192, doi:10.1016/j.msea.2007.12.010.
[28] T.P. Papageorgiou, E. Casini, H.F. Braun, T. Herrmannsdörfer, A.D. Bianchi, J. Wosnitza, J. Magn. Magn. Mater. 310 (2007) 520–522, doi:10.1016/j.jmmm.2006.10.090.
[29] C.C. Koch, Y.S. Cho, Nanostruct. Mater. 1 (1992) 207–212, doi:10.1016/0965-9773(92)90096-G.
[30] A. Ebrahimi-Purkani, S.F. Kashani-Bozorg, J. Alloys Compd. 456 (2008) 211–215, doi:10.1016/j.jallcom.2007.02.003.
[31] P. Kuziora, M. Wyszyńska, M. Polanski, J. Bystrzycki, Int. J. Hydrogen Energy 39 (2014) 9883–9887, doi:10.1016/j.ijhydene.2014.03.009.
[32] S. Rashidi, A. Ataie, Mater. Res. Bull. 80 (2016) 321–328, doi:10.1016/j.materresbull.2016.04.021.
[33] O. Maulik, D. Kumar, S. Kumar, D.M. Fabijanic, V. Kumar, Intermetallics 77 (2016) 46–56, doi:10.1016/j.intermet.2016.07.001.
[34] I. Moravcik, J. Cizek, J. Zapletal, Z. Kovacova, J. Vesely, P. Minarik, M. Kitzmantel, E. Neubauer, I. Dlouhy, Mater. Des. 119 (2017) 141–150, doi:10.1016/j.matdes.2017.01.036.
[35] D.B. Miracle, J.D. Miller, O.N. Senkov, C. Woodward, M.D. Uchic, J. Tiley, Entropy 16 (2014) 494–525, doi:10.3390/e16010494.
[36] Z. Haiping, H. Lianxi, S. Hongfei, C. Xianjue, Mater. Charact. 106 (2015) 44–51, doi:10.1016/j.matchar.2015.05.021.
[37] M. Pozuelo, C. Melnyk, W.H. Kao, J.M. Yang, J. Mater. Res. 26 (2011) 904–911, doi:10.1557/jmr.2010.94.
[38] A. Chaubey, S. Scudino, M. Khoshkhoo, K. Prashanth, N. Mukhopadhyay, B. Mishra, J. Eckert, Metals (Basel) 3 (2013) 58–68, doi:10.3390/met3010058.
[39] J. Esquivel, H. Murdoch, K. Darling, R. Gupta, Mater. Res. Lett. 6 (2018) 79–83, doi:10.1080/21663831.2017.1396262.
[40] C. Suryanarayana, Prog. Mater. Sci. 46 (2001) 1–184, doi:10.1016/S0079-6425(99)00010-9.
[41] R.K. Gupta, K.S. Darling, R.K. Singh Raman, K.R. Ravi, C.C. Koch, B.S. Murty, R.O. Scattergood, J. Mater. Sci. 47 (2012) 1562–1566, doi:10.1007/s10853-011-5986-6.
[42] R.K. Gupta, N. Birbilis, Corros. Sci. 92 (2015) 1–15, doi:10.1016/j.corsci.2014.11.041.
[43] R.K. Gupta, R.K. Singh Raman, C.C. Koch, J. Mater. Sci. 47 (2012) 6118–6124, doi:10.1007/s10853-012-6529-5.
[44] R.K. Gupta, D. Fabijanic, T. Dorin, Y. Qiu, J.T. Wang, N. Birbilis, Mater. Des. 84 (2015) 270–276, doi:10.1016/j.matdes.2015.06.120.
[45] E. Ma, Prog. Mater. Sci. 50 (2005) 413–509, doi:10.1016/j.pmatsci.2004.07.001.
[46] X. Song, J. Zhang, L. Li, K. Yang, G. Liu, Acta Mater. 54 (2006) 5541–5550, doi:10.1016/j.actamat.2006.07.040.
[47] Z.A. Munir, D.V. Quach, M. Ohyanagi, J. Am. Ceram. Soc. 94 (2011) 1–19, doi:10.1111/j.1551-2916.2010.04210.x.
[48] M. Tokita, Mechanism of spark plasma sintering Mater Science, in: Proceedings of the International Symposium on Microwave, Plasma and Thermochemical Processing of Advanced Materials, Kanagawa, 1997, pp. 69–76.
[49] J. Gonzalez-Julian, T. Kessel, M. Herrmann, J. Räthel, B. Dargatz, G. Schierning, O. Guillon, Adv. Eng. Mater. 16 (2014) 830–849, doi:10.1002/adem.201300409.
[50] A. Khalil, Z. Iqbal, A. Al-Qutub, N. Al Aqeeli, T. Laoui, R. Kirchner, N. Saheb, A.S. Hakeem, J. Nanomater. 2012 (2012) 1–13, doi:10.1155/2012/983470.
[51] J. Trapp, B. Kieback, Powder Metall. 62 (2019) 297–306, doi:10.1080/00325899.2019.1653532.
[52] R. Orrù, R. Licheri, A.M. Locci, A. Cincotti, G. Cao, Mater. Sci. Eng. R Rep. 63 (2009) 127–287, doi:10.1016/j.mser.2008.09.003.
[53] R. German, Sintering: From Empirical Obervations to Scientific Principles, Butterworth Heinemann (Elsevier), Oxford, UK, 2014. doi:10.1016/C2012-0-00717-X.
[54] Z.A. Munir, U. Anselmi-Tamburini, M. Ohyanagi, J. Mater. Sci. 41 (2006) 763–777, doi:10.1007/s10853-006-6555-2.
[55] P. Minárik, J. Stráský, J. Veselý, F. Lukáč, B. Hadzima, R. Král, J. Alloys Compd. 742 (2018) 172–179, doi:10.1016/j.jallcom.2018.01.115.
[56] W.N.A.W. Muhammad, Z. Sajuri, Y. Mutoh, Y. Miyashita, J. Alloys Compd. 509 (2011) 6021–6029, doi:10.1016/j.jallcom.2011.02.153.
[57] D. Guan, W.M. Rainforth, J. Sharp, J. Gao, I. Todd, J. Alloys Compd. 688 (2016) 1141–1150, doi:10.1016/j.jallcom.2016.07.162.
[58] M. Mondet, E. Barraud, S. Lemonnier, J. Guyon, N. Allain, T. Grosdidier, Acta Mater. 119 (2016) 55–67, doi:10.1016/j.actamat.2016.08.006.
[59] M.U.F. Khan, F. Mirza, R.K. Gupta, Materialia 4 (2018) 406–416 https://doi.org/10.1016/j.mtla.2018.10.004.
[60] A.L. Patterson, Phys. Rev. 56 (1939) 978–982.
[61] J.L. Murray, Bull. Alloy Phase Diagr. 3 (1982) 60–74, doi:10.1007/BF02873413.
[62] G.V. Raynor, The Physical Metallurgy of Magnesium and its Alloys, Pergamon Press, 1966.
[63] X.X. Li, C. Yang, T. Chen, Z.Q. Fu, Y.Y. Li, O.M. Ivasishin, E.J. Lavernia, Scr. Mater. 151 (2018) 47–52, doi:10.1016/j.scriptamat.2018.03.033.
[64] P. Villars, K. Cenzual (Eds.), Mg17Al12 Crystal Structure: Datasheet from "PAULING FILE Multinaries Edition – 2012, 2012 https://materials.springer.com/isp/crystallographic/docs/sd_0453869.
[65] M. Pozuelo, Y.W. Chang, J.M. Yang, Mater. Sci. Eng. A 594 (2014) 203–211, doi:10.1016/j.msea.2013.11.056.
[66] H. Wang, K. Zhou, G. Xie, X. Linag, W. Liang, Y. Zhao, Mater. Sci. Eng. A 560 (2013) 787–791.
[67] R.S. Mishra, Z.Y. Ma, Mater. Sci. Eng. A 67 (2005) 1–78, doi:10.1007/s11837-015-1397-5.
[68] A. Inoue, H. Kimura, K. Amiya, Mater. Trans. 43 (2002) 2006–2016, doi:10.2320/matertrans.43.2006.
[69] D. Guan, W.M. Rainforth, J. Sharp, J. Gao, I. Todd, J. Alloys Compd. 688 (2016) 1141–1150, doi:10.1016/j.jallcom.2016.07.162.
[70] S.M. Razavi, D.C. Foley, I. Karaman, K.T. Hartwig, O. Duygulu, L.J. Kecskes, S.N. Mathaudhu, V.H. Hammond, Scr. Mater. 67 (2012) 439–442, doi:10.1016/j.scriptamat.2012.05.017.
[71] Y.N. Wang, C.I. Chang, C.J. Lee, H.K. Lin, J.C. Huang, Scr. Mater. 55 (2006) 637–640, doi:10.1016/j.scriptamat.2006.06.005.
[72] J.B. Clark, Acta Metall. 16 (1968) 141–152, doi:10.1016/0001-6160(68)90109-0.
[73] J.F. Nie, Metall. Mater. Trans. A Phys. Metall. Mater. Sci. 43 (2012) 3891–3939, doi:10.1007/s11661-012-1217-2.
[74] M. Rashad, F. Pan, M. Asif, X. Chen, J. Magn. Alloy 5 (2017) 271–276, doi:10.1016/j.jma.2017.06.003.
[75] D.A. Vermilyea, C.F. Kirk, J. Electrochem. Soc. 116 (1969) 1487, doi:10.1149/1.2411579.
[76] K. Gusieva, C.H.J. Davies, J.R. Scully, N. Birbilis, Int. Mater. Rev. 60 (2015) 169–194, doi:10.1179/1743280414Y.0000000046.
[77] A.D. Sudholz, K. Gusieva, X.B. Chen, B.C. Muddle, M.A. Gibson, N. Birbilis, Corros. Sci. 53 (2011) 2277–2282, doi:10.1016/j.corsci.2011.03.010.
[78] A.D. Südholz, N. Birbilis, C.J. Bettles, M.A. Gibson, J. Alloys Compd. 471 (2009) 109–115.
[79] A.D. Südholz, N.T. Kirkland, R.G. Buchheit, N. Birbilis, Electrochem. Solid-State Lett. 14 (2011) 2010–2012, doi:10.1149/1.3523229.
[80] R.L. Liu, M.F. Hurley, A. Kvryan, G. Williams, J.R. Scully, N. Birbilis, Sci. Rep. 6 (2016) 1–12, doi:10.1038/srep28747.
[81] D. Song, A. Bin Ma, J. Jiang, P. Lin, D. Yang, J. Fan, Corros. Sci. 52 (2010) 481–490, doi:10.1016/j.corsci.2009.10.004.

[82] K.R. Kim, J.W. Ahn, G.H. Kim, J.H. Han, K.K. Cho, J.S. Roh, W.J. Kim, H.S. Kim, Met. Mater. Int. 20 (2014) 1095–1101, doi:10.1007/s12540-014-6023-5.
[83] K.D. Ralston, N. Birbilis, Corrosion 66 (2010) 1–13.
[84] D. Orlov, K.D. Ralston, N. Birbilis, Y. Estrin, Acta Mater. 59 (2011) 6176–6186, doi:10.1016/j.actamat.2011.06.033.
[85] G. Song, A. Atrens, D. St. John, L. Zheng, Magn. Alloy. Their Appl. 91 (2006) 423–431, doi:10.1002/3527607552.ch68.
[86] G.R. Argade, S.K. Panigrahi, R.S. Mishra, Corros. Sci. 58 (2012) 145–151, doi:10.1016/j.corsci.2012.01.021.
[87] J. Jiang, A. Bin Ma, N. Saito, Z. Shen, D. Song, F. Lu, Y. Nishida, D. Yang, P. Lin, J. Rare Earths 27 (2009) 848, doi:10.1016/S1002-0721(08)60348-8.
[88] G. Ben Hamu, D. Eliezer, L. Wagner, J. Alloys Compd. 468 (2009) 222–229, doi:10.1016/j.jallcom.2008.01.084.
[89] W. Xu, N. Birbilis, G. Sha, Y. Wang, J.E. Daniels, Y. Xiao, M. Ferry, Nat. Mater. 14 (2015) 1229–1235, doi:10.1038/nmat4435.